Temperature and Fluid Pressurization Effects on Frictional Stability of Shale Faults Reactivated by Hydraulic Fracturing in the Changning Block, Southwest China

Mengke An[1,2], Fengshou Zhang[1,2] (iD), Zhaowei Chen[3], Derek Elsworth[4,5] (iD), and Lianyang Zhang[6]

[1]Key Laboratory of Geotechnical and Underground Engineering of Ministry of Education, Tongji University, Shanghai, China, [2]Department of Geotechnical Engineering, College of Civil Engineering, Tongji University, Shanghai, China, [3]CNPC Engineering Technology R&D Company Limited, Beijing, China, [4]Department of Energy and Mineral Engineering, EMS Energy Institute and G3 Center, The Pennsylvania State University, University Park, PA, USA, [5]Department of Geosciences, The Pennsylvania State University, University Park, PA, USA, [6]Department of Civil and Architectural Engineering and Mechanics, University of Arizona, Tucson, AZ, USA

Abstract A shale fault reactivated during multistage hydraulic fracturing in the Changning block in the Sichuan Basin, southwest China, accompanied a cluster of small earthquakes with the largest reaching $M_L \sim 0.8$. We illuminate the underlying mechanisms of fault reactivation through measurements of frictional properties on simulated fault gouge under hydrothermal conditions. Velocity-stepping experiments were performed at a confining pressure of 60 MPa, temperatures from 30 to 300°C, pore fluid pressures from 10 to 55 MPa, and shear velocities between 0.122 and 1.22 μm/s. Results show that the gouge is frictionally strong with coefficient of friction of 0.6–0.7 across all experimental conditions. At observed in situ pore fluid pressure (30 MPa), the slip stability response is characterized by velocity strengthening at temperatures of 30–200°C and velocity weakening at temperatures of 250–300°C. Increasing the pore fluid pressure can increase values of $(a - b)$ at temperatures ≥200°C, narrowing the temperature range where velocity weakening occurs. At the in situ temperature (90°C), the simulated gouge shows only velocity strengthening behavior and aseismic slip at elevated pore fluid pressures, contrary to the observed seismicity. We postulate that the aseismic slip at elevated pore fluid pressures may trigger seismicity by activating adjacent earthquake-prone faults.

Plain Language Summary The Sichuan Basin of southwest China is the host to an increasing number of induced earthquakes potentially linked to the hydraulic fracturing for shale gas extraction. To understand whether the deep shale faults would slip unstably during hydraulic fracturing, we measure the frictional properties of powdered deep shale fault rocks (as simulated fault gouge) from a well in the Changning block in the Sichuan Basin which was identified with fault reactivation during hydraulic fracturing. We found that the simulated gouge slips stably at lower temperatures but unstably at higher temperatures. Elevating the pore fluid pressure stabilizes the fault slip at in situ and higher temperatures, contrary to the field observations. We postulate that the shale fault is prone to stable slip at higher pore fluid pressure, but this slip further can lead to the slip of adjacent unstable faults. Our results highlight the importance of combined temperature and pore fluid pressure effects on assessing the potential of induced seismicity from fluid injection activities.

1. Introduction

The Sichuan Basin of southwest China possesses rich shale gas resources with broad prospects for development (Zou et al., 2016). However, the basin is the host of an increasing number of induced earthquakes potentially linked to fluid injection for hydraulic fracturing (Chen et al., 2018; Lei et al., 2017, 2019; Meng et al., 2019). In the Changning-Weiyuan national shale gas demonstration area located in the southern edge of the basin, recorded seismicity ($M_L \geq 0$) has rapidly increased from 2009 to 2019 (Figure 1). The 2017 M_w 4.7 (Lei et al., 2017) and 2018 M_L 5.7 induced earthquakes (Lei et al., 2019) in the Changning block resulted in serious damage to nearby buildings and structures, constituting a threat to the safety of local residents.
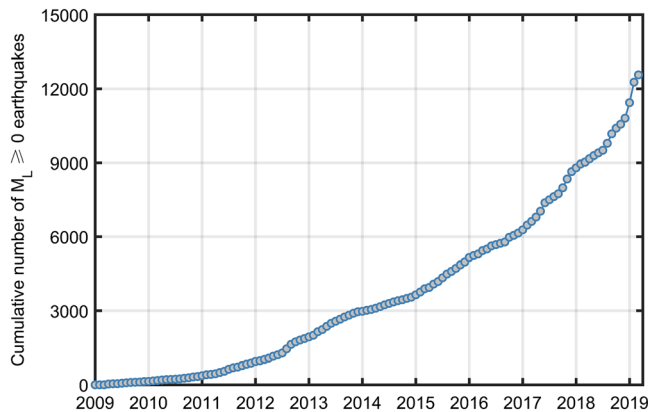
Figure 1. Cumulative number of M_L (local magnitude) ≥ 0 earthquakes in the Changning block from March 2009 to March 2019. Shale gas recovery in the Changning-Weiyuan national shale gas demonstration area started in 2011 with systematic hydraulic fracturing beginning in 2014.

Earthquakes induced during hydraulic fracturing are feasibly linked to the reactivation of pre-existing faults or fractures (Bao & Eaton, 2016; Ellsworth, 2013; Elsworth et al., 2016; Yeck et al., 2017). There are two important factors that control the slip stability of pre-existing faults or fractures during injection-related activities, namely, elevated pore fluid pressure resulting from the injection and the rate of change of pore fluid pressure (Andrés et al., 2019; French et al., 2016; Hincks et al., 2018; van der Elst et al., 2013) and high temperatures at depths of thousands of meters (Martínez-Garzón et al., 2014). The increase in pore fluid pressure can significantly decrease the effective stress and promote fault failure (Rubinstein & Mahani, 2015). Meanwhile, high temperatures can accelerate the rate of fluid-assisted processes, and the temperature difference between reservoir and injected fluid can induce a thermoelastic effect on local stress field in a reservoir, enabling the high temperature to exert a control on fault stability (Boulton et al., 2014; den Hartog et al., 2012; King & Marone, 2012; Martínez-Garzón et al., 2014). Based on observations of a reactivated shale-bearing fault during multistage hydraulic fracturing in the Changning block, Sichuan Basin, this paper explores the evolving frictional behaviors of the shale fault under hydrothermal conditions.

The fault is near injection well N201-H1 (Figure 2a), which is the first horizontal well for shale gas extraction in the Changning block. The well has a vertical depth of ~2,500 m and a total length of ~3,790 m. The Silurian Longmaxi shale is the target reservoir formation (Zhao et al., 2017). Microearthquakes occurring during the multistages fracturing of the horizontal well were monitored and recorded by eight downhole geophones that were installed in an adjacent vertical well N201 (Figure 2b). As shown in Figures 2c and 2d, the spatiotemporal characteristics of the recorded microearthquakes near the toe of the horizontal well clearly delineate a planar fault. The casing underwent severe shear deformation near this conjectured fault with the number of fracturing stages reduced from 12 to 10 as a consequence (Chen et al., 2017; Zhang, Yin, et al., 2019). Microseismic monitoring and data reduction by ant-tracking algorithms (Cox & Seitz, 2007) show that the fault has a length of ~860 m, height of ~290 m and dips 70° toward N57°E. The ant-tracking algorithm, developed by Schlumberger (Cox & Seitz, 2007), is an efficient procedure to identify, track, and sharpen the location of faults—by linking successively occurring seismic events by a trace. The depth at the top of the fault is ~2,350 m with a presumed in situ pore fluid pressure of ~32.9 MPa (equivalent pore fluid density of ~1.4 g/cm^3) and in situ temperature of ~92°C. Given the high population density (~1,000 people per km^2) in the Sichuan Basin combined with the frequent activity of hydraulic fracturing, it is important to understand the parameters that affect fault instability.

There is growing interest in understanding the mechanisms of induced seismicity associated with shale gas extraction. At room temperature, the frictional strength and stability of powdered shale gouge are dependent on the mineralogy of the gouge, primarily the phyllosilicates and organic carbon (Fang et al., 2017; Kohli & Zoback, 2013; Zhang, An, et al., 2019). With an increase in pore fluid pressure, phyllosilicate-rich shale gouges do not weaken but instead promote aseismic creep (de Barros et al., 2016; Scuderi & Collettini, 2018). Although these previous studies on the friction of shale faults or fractures highlight the effects of mineralogy and the variable stress conditions, few studies accommodate the influence of high temperature (An et al., 2020; den Hartog et al., 2012). It is not clear whether the frictional properties of powdered shale gouge change with elevated temperature and pore fluid pressure. In this regard, this paper explores the coupling effects of temperature and pore fluid pressure on the frictional properties of the powdered shale fault rocks.

2. Material and Methods

2.1. Sample Preparation

Black shale samples were recovered from rock core fragments (Figure 3) from well N201-H1 near the reactivated fault. X-ray diffraction (XRD) indicated that the simulated gouge consists of 38% quartz, 11% albite, 4% microcline, 9% calcite, 4% dolomite, 21% illite, 6% illite/smectite mixed layer, 5% chlorite, and 2% pyrite in
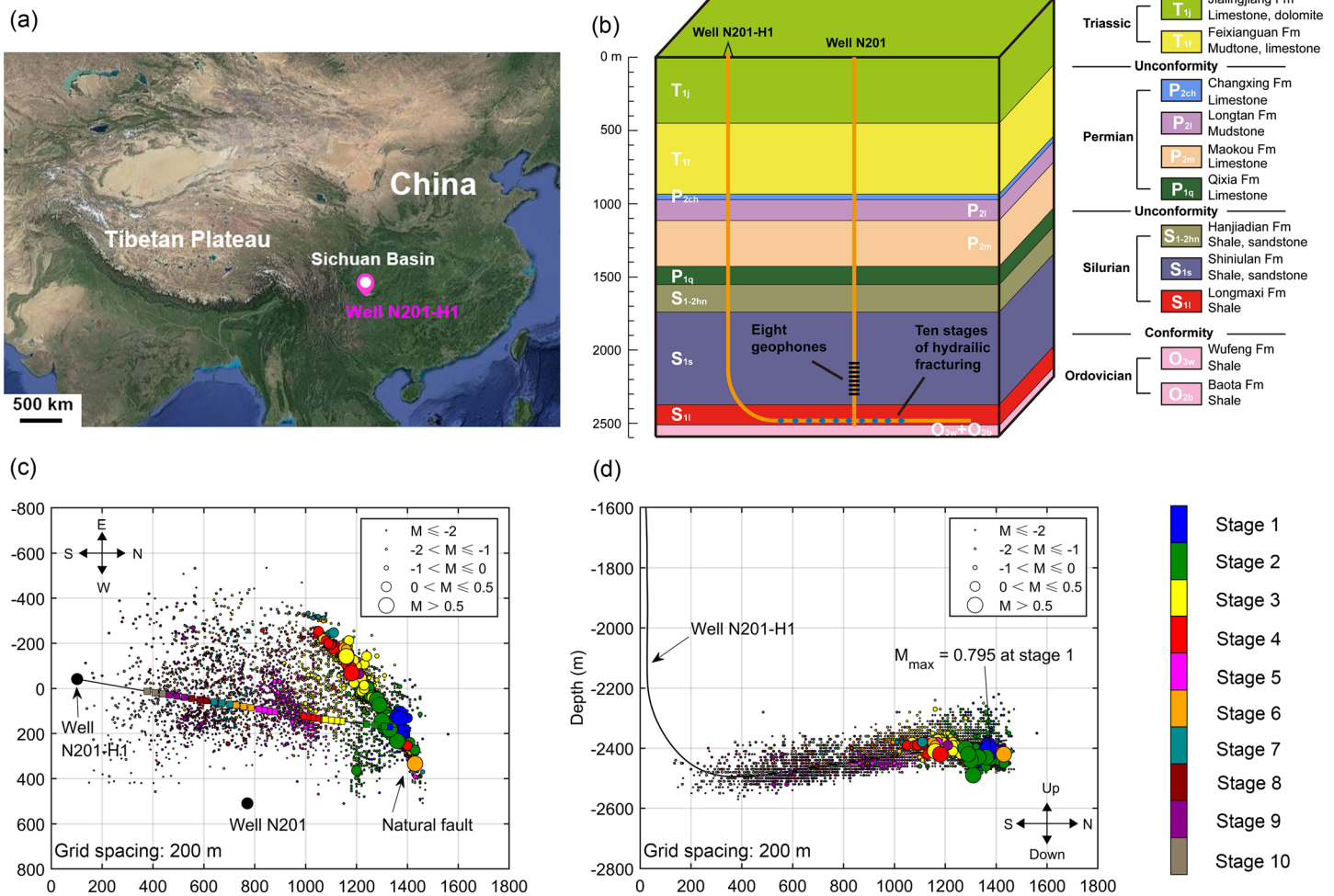
Figure 2. (a) The well N201-H1 is located at the southern edge of the Sichuan Basin, southwest China. The Sichuan Basin is adjacent to the Tibetan Plateau to the west and is one of the major shale gas production areas in China. (b) The geologic column of the region with the trajectories of wells N201 and N201-H1. The geologic strata range from Triassic through Ordovician. Eight downhole geophones were installed in the vertical well (N201) with a spacing of 30 m to record microseismicity. The deepest geophone is at ~2,305 m. (c) Top view of the recorded microearthquakes during the 10 stages hydraulic fracturing. The length of each stage is ~75–100 m, with three or four fracturing clusters for each stage. (d) Side view of the recorded microearthquakes. The size of the circles represents the moment magnitude, and the color indicates the fracturing sequence. The microseismic events during each shut-in stage were combined with the foregoing fracturing stage. The maximum moment magnitude of 0.795 occurred during the first stage.

Figure 3. Rock core fragments recovered from the reactivated shale fault.

weight. After removing the surface impurities, the cuttings were crushed and sieved to retain the <75-μm fraction as the simulated gouge. Laser particle size analysis showed that the median particle size of the gouge is 13 μm and 90 vol.% of the gouge particles have diameters <75 μm (Figure 4).

2.2. Testing Procedure

Friction experiments on the simulated gouge were conducted using a (argon) gas-confined triaxial shearing apparatus (described in detail in He et al., 2016) (Figure 5) at the Institute of Geology, China Earthquake Administration. A 1-mm-thick gouge layer was sandwiched between surfaces cut at 35° to the axis of a cylindrical stainless-steel block with a diameter of 20 mm. The forcing block surfaces are grooved (1-mm width and 0.2-mm height) perpendicular to the shearing direction. The upper forcing block is drilled with two injection holes for the transmission of pore fluids,
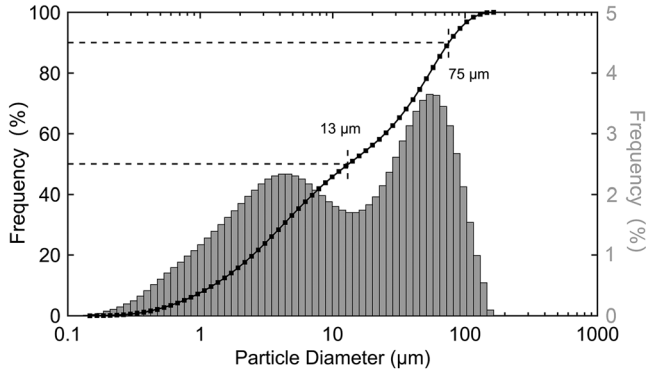
Figure 4. Particle size distribution of the simulated gouge. The 50 vol.% gouge particles are <13 μm and the 90 vol.% < 75 μm.

with a brass filter inserted into the holes to prevent gouge extrusion. Deionized water was adopted as the pore fluid to minimize chemical effects. The gouge was placed between the driving blocks, and the gouge-filled steel cylindrical blocks were inserted into a thin copper jacket with high-hardness blocks on both sides. For each experiment, the confining pressure was first applied using pressurized argon, followed by the application of pore fluid pressure. The temperature was then raised to the desired magnitude by the furnace and monitored by a thermocouple placed within the pore fluid inlet. All stress and displacement data were recorded at a sampling frequency of 1 Hz.

A total of 17 friction experiments were conducted at a confining pressure of 60 MPa (approximately equivalent to lithostatic pressure at ~2.4 km depth with rock density of ~2,500 kg/m^3) under varied pore fluid pressures and temperatures (see Table 1). The experiments are divided into three groups based on the aims of the experiments. The friction experiments in Groups 1 and 3 were performed at a constant pore fluid pressure of 30 and 55 MPa, respectively, to explore the effect of temperature on gouge friction. The friction experiments in Group 2 were carried out at a temperature of 90°C to study the role of variable pore fluid pressure on gouge friction. At the initial stage of each test, the gouge was sheared at a constant shearing velocity of 10 μm/s until steady state friction was achieved. Then, the shearing velocity was stepped between 1.22 and 0.122 μm/s with the final shear displacements reaching 3.0 to 3.5 mm (Figure 6).

2.3. Data Analysis

The frictional strength of the gouge is defined by the coefficient of friction $\mu = \tau/(\sigma_n - P_f)$ (ignoring cohesion), where τ, σ_n, and P_f are the applied shear stress, normal stress, and pore fluid pressure, respectively. For each test, the coefficient of friction was evaluated at ~2.5 mm shear displacement with 1.22 μm/s shearing velocity. The calculated stresses were corrected following the methods described in He et al. (2006) to compensate for the change in overlapping area during shearing. The velocity dependence of friction was analyzed using the rate and state friction equations with an evolution law (Dieterich, 1978, 1979; Ruina, 1983). To incorporate the effect of variable normal stress, the modified equations by Linker and Dieterich (1992) were employed, expressed as

$$\mu = \mu_0 + a\ln\left(\frac{V}{V_0}\right) + b\ln\left(\frac{V_0\theta}{d_c}\right) \tag{1}$$

$$\frac{d\theta}{dt} = 1 - \frac{V\theta}{d_c} - \frac{\alpha\theta}{b\sigma_{neff}}\frac{d\sigma_{neff}}{dt} \tag{2}$$

where μ_0 and μ are the steady state coefficients of friction measured at the reference velocity V_0 and the instantaneous velocity V, respectively, a reflects the direct effect due to a step in the shearing velocity (Figure 2a), b describes the evolution effect to a new steady state over a critical shear distance d_c (Figure 2a), θ is a state variable, α is a nondimensional parameter reflecting the effect of variable normal stress, and σ_{neff} denotes the effective normal stress. At steady state friction, the velocity dependence $(a - b)$ is calculated as

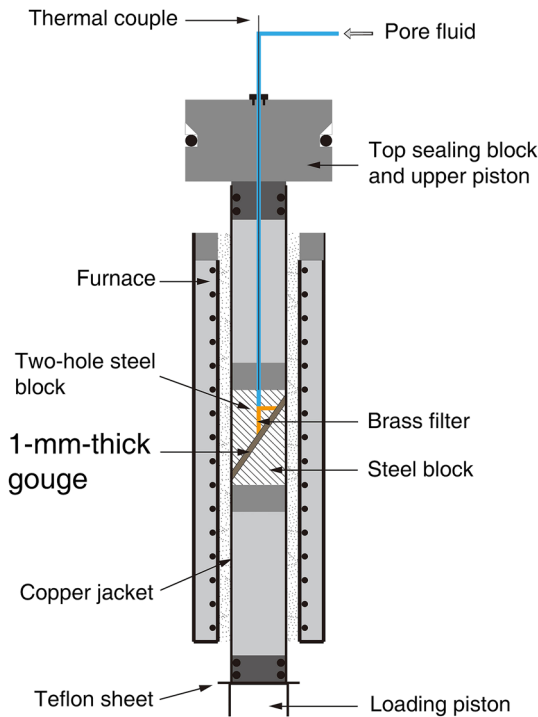$$a - b = \frac{\mu - \mu_0}{\ln(V/V_0)} \tag{3}$$

Figure 5. Schematic of the triaxial shearing assembly. Pore fluid pressure is controlled by an independent hydraulic pump. The fault assembly is wrapped in a thin copper jacket to prevent the argon gas from infiltrating into the pore space of the gouge.

Positive values of $(a - b)$ indicate velocity strengthening behavior, promoting inherently stable sliding. Conversely, gouges with negative values of $(a - b)$ show velocity weakening behavior and may

Table 1
List of Experimental Conditions and Key Data

Experiment	σ_c (MPa)	P_f (MPa)	T (°C)	μ	l_{final} (mm)	Type of motion
Data set 1: Effect of T at constant P_f = 30 MPa						
PP30-1	60	30	30	0.620	3.144	vs
PP30-2	60	30	60	0.628	3.080	vs
PP30-3	60	30	90	0.625	3.106	vs
PP30-4	60	30	120	0.641	3.015	vs
PP30-5	60	30	150	0.640	3.148	vs
PP30-6	60	30	200	0.630	3.565	vs
PP30-7	60	30	250	0.635	3.508	vw
PP30-8	60	30	300	0.664	3.485	vw
Data set 2: Effect of P_f at constant T = 90°C						
T90-1	60	10	90	0.600	3.215	vs
T90-2	60	20	90	0.604	3.185	vs
T90-3	60	40	90	0.601	3.215	vs
T90-4	60	50	90	0.667	3.065	vs
T90-5	60	55	90	0.680	2.944	vs
Data set 3: Effect of T at constant P_f = 55 MPa						
PP55-1	60	55	150	0.636	3.450	vs
PP55-2	60	55	200	0.609	3.450	vs
PP55-3	60	55	250	0.680	3.500	vs
PP55-4	60	55	300	0.649	3.495	vw

Note. σ_c = confining pressure, P_f = pore fluid pressure, T = temperature, μ = coefficient of friction, l_{final} = final shearing displacement, vs = velocity strengthening, vw = velocity weakening.

experience unstable sliding once critical stiffness is met. Other frictional constitutive parameters were estimated using an iterative least squares method by incorporating Equations 1 and 2 and a formulation describing the elastic interactions with the testing machine (Marone, 1998). The first velocity step may not be truly representative of the ultimate steady state—correspondingly, it is excluded. All frictional constitutive parameters were calculated from the second velocity step. After the shear experiments, the deformed gouge samples were first dried at room temperature for 2 days. Next, the deformed gouges were impregnated with epoxy resin in a vacuum before slicing into thin sections perpendicular to the shear direction and along the sample axis. The thin sections were polished and coated with carbon for microstructural characterization using scanning electron microscopy (SEM) (instrument type: Zeiss-sigma).

3. Results

3.1. Mechanical Data

Each test exhibits a nearly linear increase of friction in the first ~0.5 mm of shear displacement, followed by either a slip strengthening or slip weakening behavior (Figures 6a and S1 in the supporting information). The coefficients of friction of the gouge at varied temperatures and pore fluid pressures are in the range 0.60–0.70 (Figure 6b and Table 1). As shown in Figure 6b, at P_f = 30 MPa, the coefficient of friction only increases from 0.62 to 0.66 when T is increased from 30 to 300°C, implying that the temperature just has a minor influence on the gouge friction. One can also see that the coefficient of friction of the gouge slightly depends on the variation of pore fluid pressure—with higher coefficients of friction (μ = 0.67–0.68) apparent at the highest pore fluid pressures (P_f = 50 or 55 MPa) (Figure 6b). The variations of effective normal stress in representative experiments are shown in Figure S2.

The simulated gouge exhibits positive values of $(a - b)$ at $T \leq 200$°C and varied pore fluid pressures (Figure 7 and Table S1). A transition from velocity strengthening behavior $(a - b > 0)$ to velocity weakening behavior $(a - b < 0)$ can be identified at T = 250°C and P_f = 30 MPa (Figure 7a), similar to the results of den Hartog et al. (2012) on simulated illite-quartz gouge (velocity strengthening at T = 150–250°C and velocity weakening at T = 250–400°C). However, at P_f = 55 MPa, values of $(a - b)$ are positive at T = 250°C and become negative when T reaches 300°C (Figure 7a). This indicates that, at the same testing temperature of 250°C, the gouge becomes more stable at elevated pore fluid pressures. However, at T = 90°C, the values of $(a - b)$ barely changes with pore fluid pressures (Figure 7b). The frictional parameters a, b, and d_c with
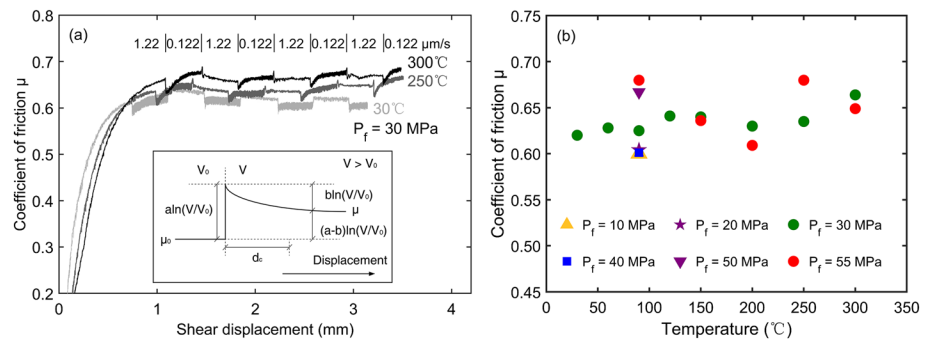

Figure 6. (a) Coefficient of friction μ versus shear displacement from representative experiments at a pore fluid pressure of 30 MPa. The inset in (a) shows the rate and state friction parameters. The strain weakening effect was corrected by detrending the slope in the calculation of $(a - b)$. (b) Measured coefficient of friction μ versus temperatures at different pore fluid pressures.
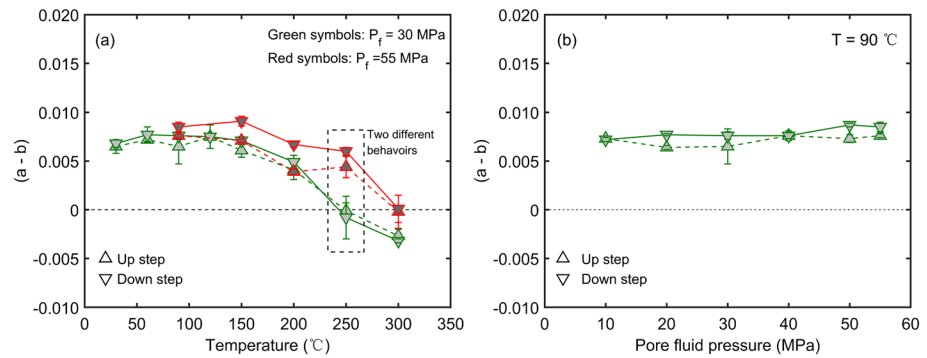
Figure 7. Variation of $(a - b)$ with (a) temperature at $P_f = 30$ and 55 MPa, respectively, and (b) pore fluid pressure at $T = 90°C$. The velocity up and down steps represent step magnitudes of 0.122–1.22 and 1.22–0.122 µm/s, respectively. The plotted $(a - b)$ is the average value from the same velocity steps in each test with error derived from the standard deviation.

respect to temperature and pore fluid pressure are further compared. At $P_f = 30$ and 55 MPa (Figures 8a and 8c), the values of a barely change with temperature, while the values of b show a rapid increase at $T \geq 200°C$. The responses of values of a or b at higher temperatures are significantly different in previous laboratory measurements (den Hartog et al., 2012; He et al., 2016; Lu & He, 2018; Zhang, He, et al., 2017), possibly due to the variation in gouge materials and testing conditions. The increase in values of $(a - b)$ at $T \geq 200°C$ is caused by independent changes in values of a and of b. Values of d_c obtained in velocity up steps show a decreasing trend at $T \geq 200°C$, but those obtained in velocity down steps increase with higher temperature at $T \geq 200°C$ (Figure 8e). At $T = 90°C$, both values of a and b exhibit a slightly increasing trend with an increase in pore fluid pressure, but the values of d_c are barely affected by the pore fluid pressure (Figures 8b, 8d, and 8f).

3.2. Microstructural Characterization

Microstructures of deformed samples were characterized using scanning electron microscopy (SEM) in backscattering mode. Methods of Logan et al. (1992) were adopted to define the fabric of the fault zones and to describe gouge fabrics. The fabrics of gouge samples returning velocity strengthening behavior are different from those returning velocity weakening responses. At $P_f = 30$ MPa and lower temperatures of 30 and 90°C (Figures 9a, 9b, and 10), the gouges exhibited velocity strengthening response, and the microstructures of the deformed gouges show apparent particle crushing and elongated clays, with a moderately sheared zone (MSR, with larger particles) in the center of the gouge sample and an intensely sheared zone (ISR, with smaller particles) distributed along the upper and lower boundaries. When the temperature is increased to 250 and 300°C (Figures 9c and 9d), the gouges exhibited velocity weakening response, and Y-oriented and R1-oriented shears develop together with a localized zone with finely comminuted particles. In contrast, when the pore fluid pressure is increased to $P_f = 55$ MPa (Figures 9e and 9f), the deformed gouge samples show a homogeneous shear mode with no apparent particle crushing and only minor Y-oriented shears, possibly due to the lower effective stress.

4. Discussion

4.1. Mechanisms of Combined T and P_f Effects on Fault Stability

The current experiments on powdered shale fault rock at $P_f = 30$ MPa and $T = 30–300°C$ exhibit two regimes of velocity dependence $(a - b)$—these are velocity strengthening behavior $(a - b > 0)$ at $T = 30–200°C$ and velocity weakening behavior $(a - b < 0)$ at $T = 250–300°C$ (Figure 7a). The discrepancy of d_c values between velocity up and down steps is attributed to healing and the difference in the post shear velocities. The agreement with den Hartog et al. (2012) in the temperature at which velocity strengthening changes to weakening is probably coincidental—due to the differences in gouge material and experimental conditions (especially the different effective normal stress). When the pore fluid pressures increase from 30 to 55 MPa, the temperature range for velocity weakening behavior narrows from $T = 250–300°C$ to only $T = 300°C$ (Figure 7a). These results suggest that the frictional stability of the gouge is controlled by the coupled effect of temperature and pore fluid pressure.
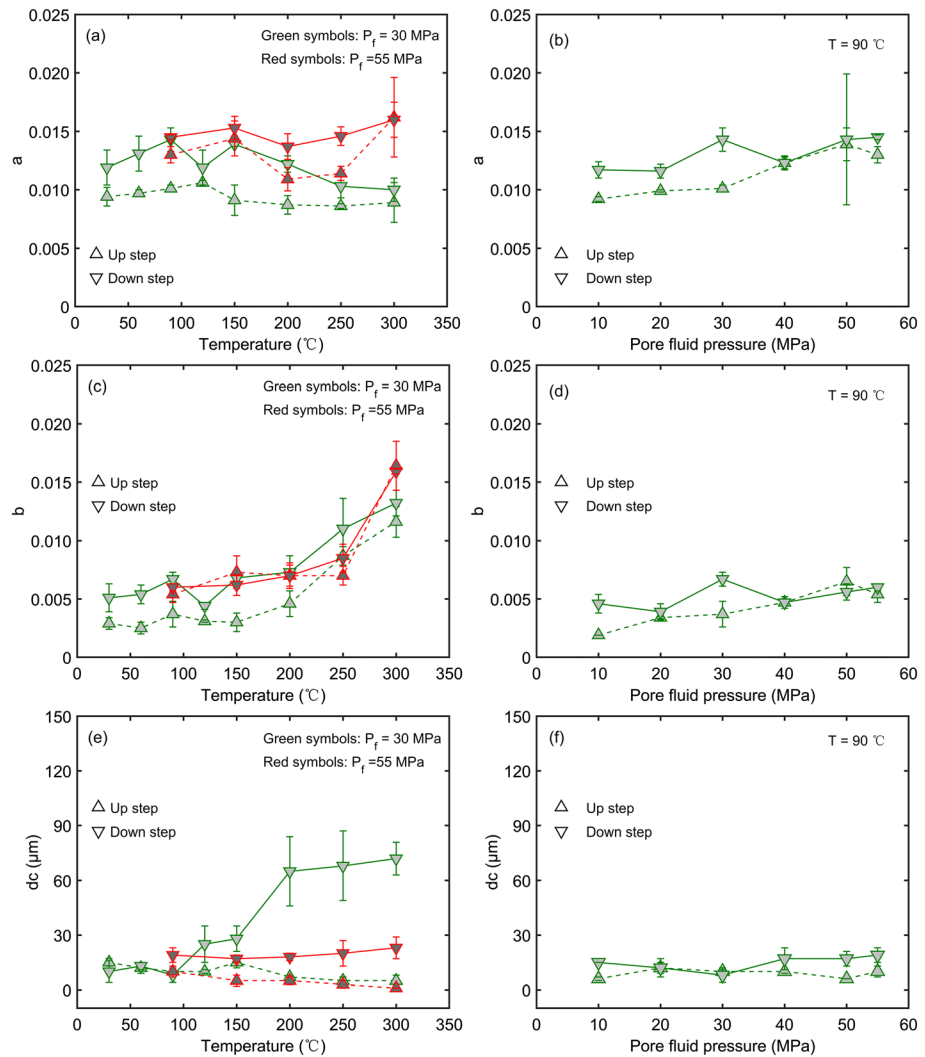
Figure 8. Summary of frictional constitutive parameters a, b, and d_c. (a) The direct effect a, (c) the evolution effect b, and (e) the critical slip distance d_c at different temperatures (30–300°C) for $P_f = 30$ and 55 MPa. (b) The direct effect a, (d) the evolution effect b, and (f) the critical slip distance d_c at different pore fluid pressures (10–55 MPa) and $T = 90$°C. Velocity up and down steps represent the velocity magnitudes of 0.122–1.22 and 1.22–0.122 μm/s, respectively. The plotted frictional constitutive parameters are the average values from the same velocity steps in each test with the error calculated from the standard deviation.

The changes in velocity dependence $(a - b)$ with temperature can be partially explained by using the microphysical model for quartz-phyllosilicate gouges (den Hartog & Spiers, 2014; den Hartog et al., 2012). According to the microphysical model, two processes, that is, shear-induced gouge dilation and thermally activated gouge compaction possibly by pressure solution, may control the friction velocity dependence. At higher temperatures ($T = 250$–300°C) and for steady state friction (immediately before the velocity step), thermally activated gouge compaction is stronger due to the action of pressure solution of quartz minerals and a denser gouge structure will be formed than at lower temperatures ($T = 30$–200°C). The denser structure at higher temperatures may accentuate gouge dilation (Paterson, 1995) upon application of a velocity up step. This dilation dominates any compaction at the higher shearing velocity, retains elevated porosity and results in a decrease in the macroscopic frictional strength (Samuelson et al., 2009)—contributing to the observed velocity weakening behavior. Although we do not directly measure the variation in gouge porosity, this explanation for gouge weakening is a reasonable speculation and has been previously employed in interpreting laboratory observations (e.g., Boulton et al., 2014; Sawai et al., 2016). Meanwhile, at higher temperatures ($T = 250$–300°C), the increase in porosity at a velocity up step may indicate an increase in the evolution
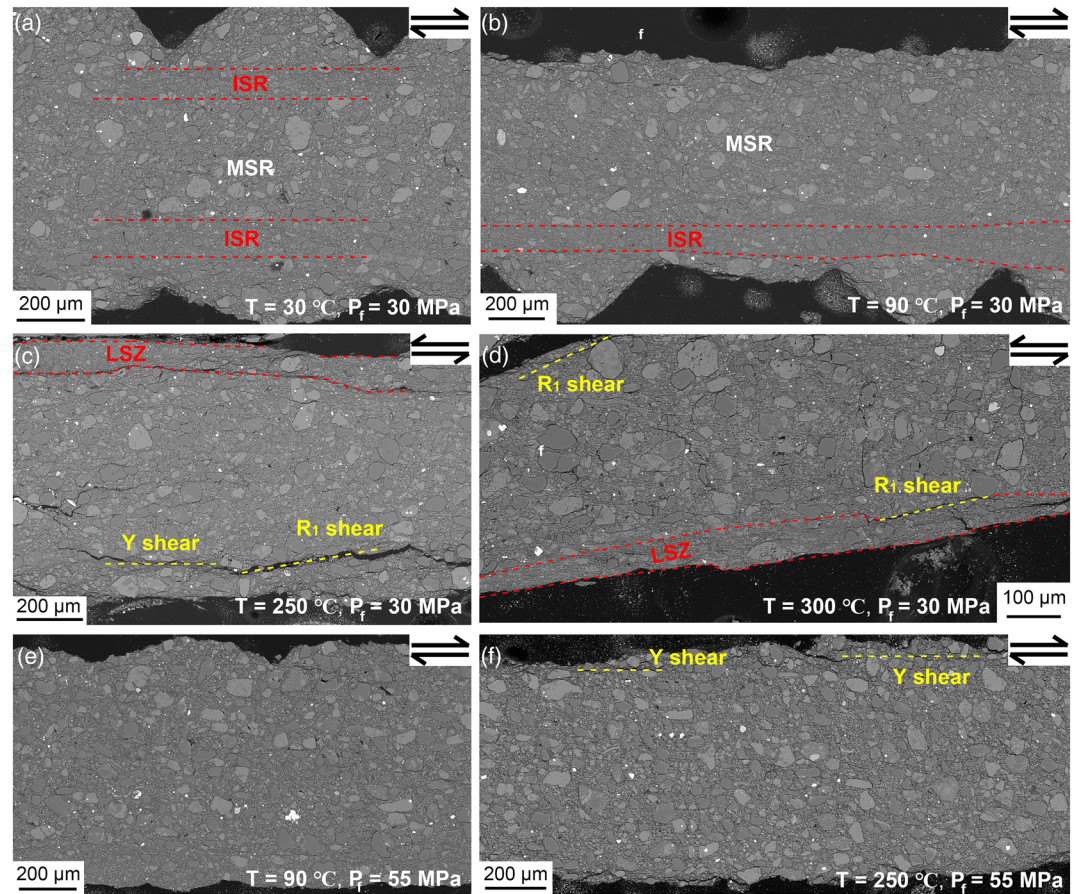
Figure 9. Microstructures of representative deformed gouge samples (backscattered images) with the features described by the method of Logan et al. (1992). (a) At $T = 30°C$, $P_f = 30$ MPa, an intensely sheared region (ISR, red dashed lines) shows an apparent grain size reduction than in the moderately sheared region (MSR). (b) At $T = 90°C$, $P_f = 30$ MPa. (c) At $T = 250°C$, $P_f = 30$ MPa, a localized shear zone (LSZ, red dashed lines) can be observed on the boundary with very fine particles. (d) At $T = 300°C$, $P_f = 30$ MPa, a localized shear zone (red dashed lines) can be seen in the R1 shear direction. (e) At $T = 90°C$, $P_f = 55$ MPa. (f) At $T = 250°C$, $P_f = 55$ MPa. The gouge samples in (a), (b), (e), and (f) exhibited velocity strengthening behavior, and gouges in (c) and (d) exhibited velocity weakening response.

effect (b value) since the evolution effect is associated with the creation of new grain-grain contacts (Niemeijer & Spiers, 2007). Our results indeed show that the values of b increase with the increasing temperatures at $T = 250–300°C$ (Figure 8c). The evolution effect (Figure 8c) and the development of a shear localization zone (Figures 9c and 9d) at $T = 250–300°C$ can be partially understood from the observations of Marone et al. (1990). When the shear stress approaches about one-quarter of the peak shear stress, the gouge begins to dilate with progressive shear straining until reaching the peak shear stress. Post peak (stress/strength) change in porosity with the shear strain decreases with a decrease in shear stress, leading to a decrease in dilation rate that accompanies shear localization (Marone et al., 1990). Our experiments only exhibit localized shear (Figure 9) in the velocity weakening behavior gouges. However, localized shear is also reported in gouges with velocity strengthening behavior (He et al., 2016). We postulate that the absence of localized shear in our tested gouges (with velocity strengthening behavior) results from the high content of phyllosilicate minerals and weak pressure solution of quartz at lower temperatures (den Hartog et al., 2012; He et al., 2016).

At the in situ temperature (90°C), the pore fluid pressure for the shear experiments was varied from 10 to 55 MPa—specifically to explore the effect of pore fluid pressure. These pressures are representative of the fluid injection phase where massive hydraulic fracturing occurs (Ellsworth, 2013; Rubinstein & Mahani, 2015) and of long-term reservoir depletion from gas production. A confining pressure of 60 MPa
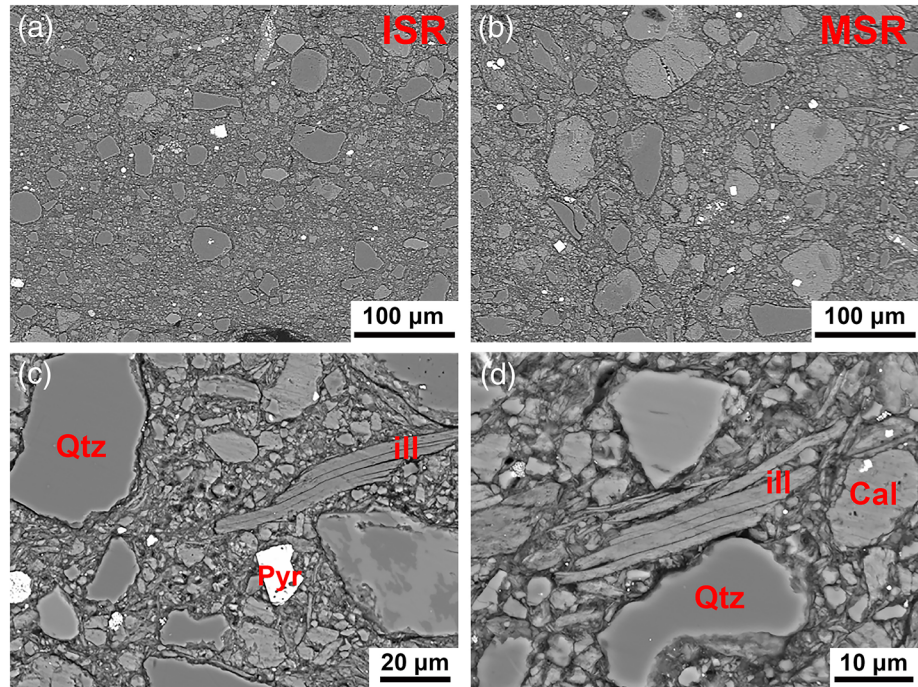
Figure 10. Microstructures of deformed gouge sample at $\sigma_c = 60$ MPa, $P_f = 30$ MPa, and $T = 90$°C (Figure 9b). (a) and (b) Comparison of the intensely sheared zone (ISR) and moderately sheared zone (MSR). (c) and (d) Elongated clay minerals in the deformed gouge. Minerals: Qtz = quartz, ill = illite, Pyr = pyrite, Cal = calcite.

functionally limits pore fluid pressures to 55 MPa. From Figure S2, the effective normal stress is 10–15 MPa at the highest pore fluid pressure. At this condition, the highest pore fluid pressure is a factor of two larger than the in situ pore fluid pressure—representative of injection operations (Chang et al., 2020). The lower pore fluid pressures (10 and 20 MPa) are representative of reservoir depletion (Buijze et al., 2019). However, elevating the pore fluid pressure alone did not significantly influence the frictional stability of the tested gouge (Figure 7b), at least at an in situ temperature (90°C)—an important observation.

Based on a simple spring-slider model, the prerequisites for fault instability are that the fault exhibits rate-weakening response $(a - b < 0)$ and that the slider stiffness K is smaller than the critical stiffness K_{cr} (Rice & Ruina, 1983), expressed by

$$K < K_{cr} = \frac{(\sigma_n - P_f)(b - a)}{d_c} \tag{4}$$

According to Equation 4, for a rate-weakening fault with negative values of $(a - b)$, decreasing the effective normal stress can lower the critical stiffness and thus stabilize the fault zone. However, as shown in Figure 7a, the values of $(a - b)$ at $P_f = 55$ MPa are larger than those at $P_f = 30$ MPa at $T \geq 250$°C with opposite responses at $T = 250$°C (velocity weakening at $P_f = 30$ MPa and velocity strengthening at $P_f = 55$ MPa) are shown. This arises since the effective normal stress exerts a control on both the velocity dependence $(a - b)$ and the critical stiffness K_{cr}. By employing the above-mentioned microphysical model (den Hartog & Spiers, 2013; Niemeijer & Spiers, 2007), decreasing the effective normal stress would decrease the rate of gouge compaction or dilation and is similar to the effects of lowering the temperature. This will shift the transition temperature to a higher value.

4.2. Laboratory-Measured Gouge Velocity Strengthening Versus In Situ Seismicity

An important question remaining is why the powdered shale rocks exhibit velocity strengthening behavior under recreated in situ conditions ($T = 90$°C, $P_f = 30$ MPa) and where elevating the pore fluid pressure would also favor aseismic slip at $T = 90$°C (Figure 7b)—but induced seismic events are abundant during
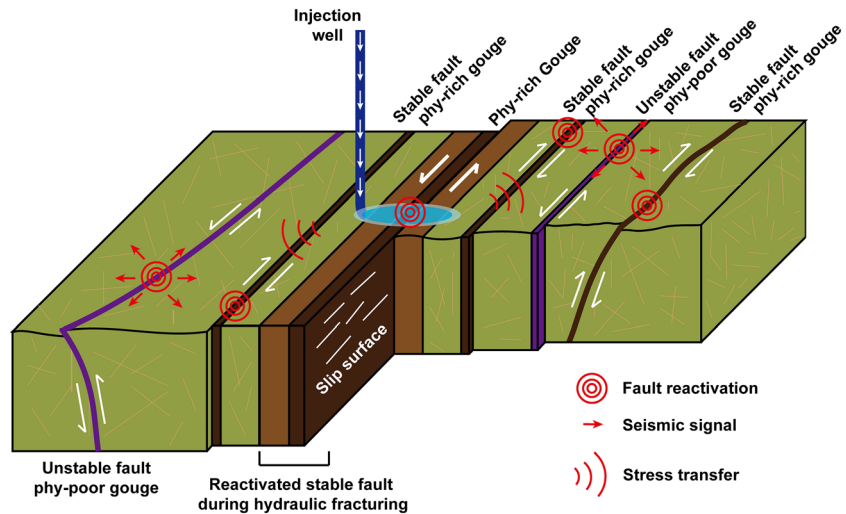
Figure 11. Schematic of fault response to hydraulic fracturing. The blue elliptical area close to the injection well indicates the footprint of the hydraulic fracturing. Subsurface faults may slip either stably or unstably as a result of strata heterogeneity. Phy represents the phyllosilicate minerals. Hydraulic fracturing may directly reactivate a stable fault (with phyllosilicate-rich gouge) (brown) with the stress transfer facilitating the failure of adjacent unstable faults (phyllosilicate-poor gouge) (purple), finally triggering seismicity.

the multistage hydraulic fracturing (Figures 2c and 2d). We realize that the gouge material (likely clay-dominated) along the fault surfaces may not be identical to that tested in the laboratory and that the laboratory experiments are not a perfect representation of nature—in particular, the imposed slip velocities are likely significantly higher than those in nature. However, previous laboratory friction or large-scale in situ experiments and modeling studies (Bhattacharya & Viesca, 2019; Cappa et al., 2018, 2019; Guglielmi et al., 2015; Scuderi & Collettini, 2018) have indicated that slow but accelerating slip or aseismic creep are observed at elevated pore fluid pressures, highlighting the importance of fluid diffusion processes. Fault creep at high pore fluid pressures may modify the local stress distribution, and this stress reorientation may activate adjacent faults (Rubinstein & Mahani, 2015; Zhang, Fang, et al., 2017). Subsurface heterogeneity, especially the variation in mineralogy and geological structure, may also play an important role in promoting triggered seismicity (Cappa et al., 2019; Scuderi et al., 2017). Reservoir shales generally span a wide range of mineral compositions but can be indexed into three key groups of minerals—tectosilicates, phyllosilicates, and carbonates (Kohli & Zoback, 2013). Tectosilicate-rich or carbonate-rich shale gouges can facilitate unstable fault slip, while phyllosilicate-rich shale gouges are prone to enhance aseismic creep (Chen et al., 2015a, 2015b; Fang et al., 2018; Kohli & Zoback, 2013). In addition, aseismic fault creep may activate unstable faults and trigger the seismicity (Elsworth et al., 2016; Lei et al., 2017), as illustrated in Figure 11. Based on the mineralogical analysis on the core samples from the exploration wells (Jiang et al., 2016; Xu et al., 2019), the Lower Silurian Longmaxi Formation shale shows a strong variation in mineral compositions, with quartz content in the range 20–60% and clay content in the range 15–65%. This strong variation in mineralogy indicates the possibility of both brittle and ductile faults in the Longmaxi Formation shale. In addition, the anticlinal and synclinal geological structures are widely developed in Sichuan Basin (Guo, 2013; Tan et al., 2014) and further increase strata complexity. Under perturbed stress conditions (e.g., by injection of pressurized fluid), faults rich in weak minerals can presumably deform predominantly by creep. The full spectrum of fault deformation modes during fracturing may not be fully displayed.

The seismicity resulting from hydraulic fracturing clearly extends into the Shiniulan formation (Figure 2). This indicates that the earthquakes could also be induced at the upper/lower formation of the reservoir. The Shiniulan formation contains shale, sandstones, and carbonates (Xu et al., 2019) with the sandstone and carbonate gouges potentially unstable at in situ conditions on the basis of previous laboratory results (Chen et al., 2015b; Hunfeld et al., 2017; Zhang, An, et al., 2019). Based on the model of Eyre et al. (2019), distal fault rupture (e.g., in Shiniulan formation) may result from aseismic fault slip generated within the reservoir (e.g., in Longmaxi formation), highlighting the importance of fault aseismic slip.
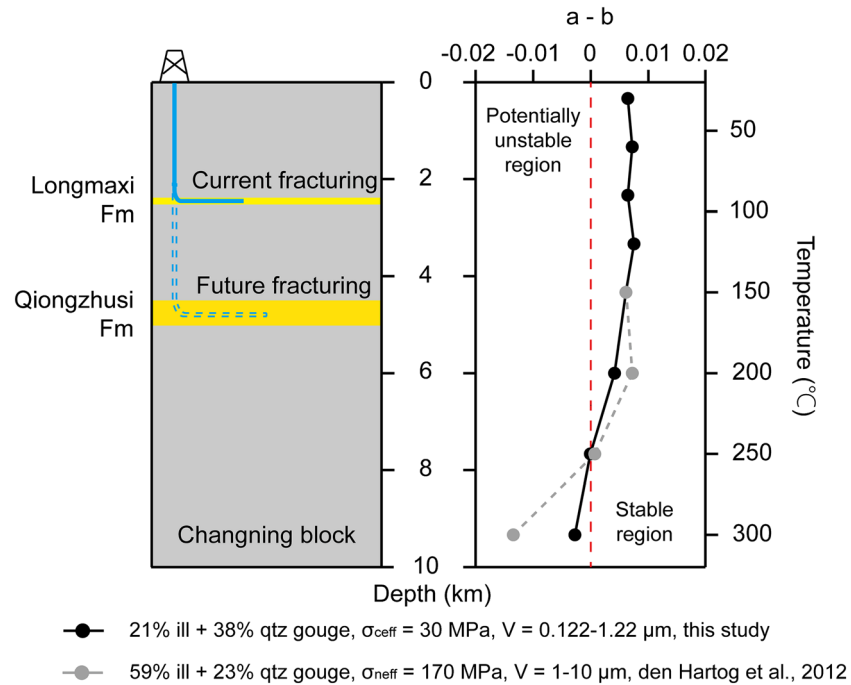
Figure 12. Magnitude of $(a - b)$ versus depth and temperature in the Changning block of the Sichuan Basin. The current target hydraulic fracturing zone is the Lower Silurian Longmaxi Formation at a depth of 2.3–2.5 km (blue solid line to the left), while future target hydraulic fracturing zones will extend to the Lower Cambrian Qiongzhusi Formation at a depth of 4.5–5.0 km (blue dashed line to the left) (Xu et al., 2019). The black solid line with black circles (to the right) shows the variation of $(a - b)$ with temperature for 21% illite (ill) + 38% quartz (qtz) gouge in this study, and the gray dashed line with gray circles (right) represents the results of den Hartog et al. (2012). The regions with $(a - b) > 0$ and $(a - b) < 0$ denote the inherent stable and potentially unstable regions, respectively, for gouge-filled faults. σ_{ceff} = effective confining stress, σ_{neff} = effective normal stress.

Importantly, our results indicate that the fault gouge cannot be the origin of the seismicity at the projected in situ P, T conditions—even though the events are aligned and broadly coincident with a pre-existing fault. The alignment of the observed seismicity in the vicinity of the fault suggests that since only aseismic deformation can occur within the fault core (our tested gouge) this then overloads rough fractures (containing bridging asperities) within the fault damage zone—resulting in the transition from an original aseismic signal to a seismic signal, consistent with field observations elsewhere (Guglielmi et al., 2015). It is the impact of this off-fault structure in the damage zone that results in the seismicity—speculated to result from the strain weakening breakage of asperities on the fractures comprising the damage zone.

4.3. Implications for Fault Behavior During Hydraulic Fracturing

Our results have important implications for understanding the friction of shale-bearing faults in the Changning block of the Sichuan Basin and controls on induced seismicity during fracturing relative to different temperatures and pore fluid pressures. We consider a temperature gradient of 30°C/km in the Changning block, based on previous observations (24–36°C/km in Changning-Weiyuan national shale gas demonstration area) (Xi et al., 2018) and this study (92°C at 2,350 m). Current fracturing at a depth of 2,300–2,500 m with a temperature of 90–100°C (ground surface temperature of 20°C) and future fracturing at a recovery depth reaching to 4,500–5,000 m at a temperature of 160–170°C may not directly destabilize the illite-quartz dominated and illite-rich shale gouges (den Hartog et al., 2012) (Figure 12). Although we cannot exclude the possibility of brittle layers in shales (Fang et al., 2018; Kohli & Zoback, 2013), the results in Figure 12 demonstrate that the temperature alone may not be the main factor contributing to seismicity in the shallow reservoirs and highlights the importance of pore fluid pressures. Meanwhile, high temperature may assist fluid-related processes and modulate the local stresses (Martínez-Garzón et al., 2014; Westaway & Burnside, 2019). Hence, the combined effect of temperature and pore fluid pressure is important in triggering seismicity in the shallow shale reservoirs.

In addition, other compounding factors cannot be neglected in the observed triggering of earthquakes, including the presence of earthquake-prone rock types and in situ driving slip rates. Based on previous laboratory results (Chen et al., 2015b; Pluymakers & Niemeijer, 2015), carbonate or anhydrite gouges are potentially unstable at current in situ reservoir conditions. Interbedded dolomites and gypsum-rich strata are present between the Longmaxi and Qiongzhusi Formations in the Changning block, Sichuan Basin, southwest China (Xu et al., 2019). Similarly, the natural driving slip rates of the faults are much lower than those utilized in the laboratory. Lowering the driving velocity may reduce frictional stability, that is, induce smaller values of $(a - b)$ (Chen et al., 2015a).

5. Conclusions

We examined the coupling effects of high temperature and elevated pore fluid pressure on the frictional properties of powdered shale rocks from a reactivated fault during multistage hydraulic fracturing in Changning block, Sichuan Basin, southwest China. The results demonstrate that temperature has a significant effect on the frictional response of the powdered shale gouge. At a pore fluid pressure of 30 MPa, the gouge undergoes a transition from velocity strengthening to weakening behavior at a temperature of 250°C. Elevating the pore fluid pressure may stabilize the shale-bearing fault at the studied temperature range from 30 to 300°C. We interpret that aseismic creep at elevated pore fluid pressure may have triggered the observed microearthquakes by changing the local stress distribution and reactivating the adjacent unstable faults. Our results shed light on the possible mechanisms for induced microearthquakes from shale-bearing faults during multistage hydraulic fracturing and have important implications for better understanding the occurrence of hydraulic fracturing induced seismicity.

Data Availability Statement

The earthquake data in Changning block and all friction constitutive data in this work are available online (https://doi.org/10.5061/dryad.5tb2rbp0s).

References

An, M., Huang, H., Zhang, F., & Elsworth, D. (2020). Effect of slick-water fracturing fluid on the frictional properties of shale reservoir rock gouges. *Geomechanics and Geophysics for Geo-Energy and Geo-Resources*, *6*(1), 1–16. https://doi.org/10.1007/s40948-020-00153-1

Andrés, S., Santillán, D., Mosquera, J. C., & Cueto-Felgueroso, L. (2019). Delayed weakening and reactivation of rate-and-state faults driven by pressure changes due to fluid injection. *Journal of Geophysical Research: Solid Earth*, *124*, 11,917–11,937. https://doi.org/10.1029/2019JB018109

Bao, X., & Eaton, D. W. (2016). Fault activation by hydraulic fracturing in western Canada. *Science*, *354*(6318), 1406–1409. https://doi.org/10.1126/science.aag2583

Bhattacharya, P., & Viesca, R. C. (2019). Fluid-induced aseismic fault slip outpaces pore-fluid migration. *Science*, *364*(6439), 464–468. https://doi.org/10.1126/science.aaw7354

Boulton, C., Moore, D. E., Lockner, D. A., Toy, V. G., Townend, J., & Sutherland, R. (2014). Frictional properties of exhumed fault gouges in DFDP-1 cores, Alpine Fault, New Zealand. *Geophysical Research Letters*, *41*, 356–362. https://doi.org/10.1002/2013GL058236

Buijze, L., van den Bogert, P. A. J., Wassing, B. B. T., & Orlic, B. (2019). Nucleation and arrest of dynamic rupture induced by reservoir depletion. *Journal of Geophysical Research: Solid Earth*, *124*, 3620–3645. https://doi.org/10.1029/2018JB016941

Cappa, F., Guglielmi, Y., Nussbaum, C., & Birkholzer, J. (2018). On the relationship between fault permeability increases, induced stress perturbation, and the growth of aseismic slip during fluid injection. *Geophysical Research Letters*, *45*, 11,012–11,020. https://doi.org/10.1029/2018GL080233

Cappa, F., Scuderi, M. M., Collettini, C., Guglielmi, Y., & Avouac, J. (2019). Stabilization of fault slip by fluid injection in the laboratory and in situ. *Science Advances*, *5*, 1–9. https://doi.org/10.1126/sciadv.aau4065

Chang, K. W., Yoon, H., Kim, Y., & Lee, M. Y. (2020). Operational and geological controls of coupled poroelastic stressing and pore-pressure accumulation along faults: Induced earthquakes in Pohang, South Korea. *Scientific Reports*, *10*(1), 1, 2073–12. https://doi.org/10.1038/s41598-020-58881-z

Chen, H., Meng, X., Niu, F., Tang, Y., Yin, C., & Wu, F. (2018). Microseismic monitoring of stimulating shale gas reservoir in SW China: 2. Spatial clustering controlled by the preexisting faults and fractures. *Journal of Geophysical Research: Solid Earth*, *123*, 1659–1672. https://doi.org/10.1002/2017JB014491

Chen, J., Verberne, B. A., & Spiers, C. J. (2015a). Effects of healing on the seismogenic potential of carbonate fault rocks: Experiments on samples from the Longmenshan Fault, Sichuan, China. *Journal of Geophysical Research: Solid Earth*, *120*, 5479–5506. https://doi.org/10.1002/2015JB012051

Chen, J., Verberne, B. A., & Spiers, C. J. (2015b). Interseismic re-strengthening and stabilization of carbonate faults by "non-Dieterich" healing under hydrothermal conditions. *Earth and Planetary Science Letters*, *423*, 1–12. https://doi.org/10.1016/j.epsl.2015.03.044

Chen, Z., Shi, L., & Xiang, D. (2017). Mechanism of casing deformation in the Changning–Weiyuan national shale gas demonstration area and countermeasures. *Natural Gas Industry B*, *4*(1), 1–6. https://doi.org/10.1016/j.ngib.2017.07.001

Cox, T., & Seitz, K. (2007). *Ant tracking seismic volumes for automated fault interpretation* (Vol. 670571). Paper presented at CSPG CSEG Convention, Alberta.

de Barros, L., Daniel, G., Guglielmi, Y., Rivet, D., Caron, H., Payre, X., et al. (2016). Fault structure, stress, or pressure control of the seismicity in shale? Insights from a controlled experiment of fluid-induced fault reactivation. *Journal of Geophysical Research: Solid Earth*, *121*, 4506–4522. https://doi.org/10.1002/2015JB012633

den Hartog, S. A. M., Niemeijer, A. R., & Spiers, C. J. (2012). New constraints on megathrust slip stability under subduction zone P–T conditions. *Earth and Planetary Science Letters*, *353–354*, 240–252. https://doi.org/10.1016/j.epsl.2012.08.022

den Hartog, S. A. M., & Spiers, C. J. (2013). Influence of subduction zone conditions and gouge composition on frictional slip stability of megathrust faults. *Tectonophysics*, *600*, 75–90. https://doi.org/10.1016/j.tecto.2012.11.006

den Hartog, S. A. M., & Spiers, C. J. (2014). A microphysical model for fault gouge friction applied to subduction megathrusts. *Journal of Geophysical Research: Solid Earth*, *119*, 1510–1529. https://doi.org/10.1002/2013JB010580

Dieterich, J. H. (1978). Time-dependent friction and the mechanics of stick-slip. *Pure and Applied Geophysics*, *116*(4–5), 790–806. https://doi.org/10.1007/BF00876539

Dieterich, J. H. (1979). Modeling of rock friction: 1. Experimental results and constitutive equations. *Journal of Geophysical Research*, *84*(B5), 2161. https://doi.org/10.1029/JB084iB05p02161

Ellsworth, W. L. (2013). Injection-induced earthquakes. *Science*, *341*(6142), 1225942. https://doi.org/10.1126/science.1225942

Elsworth, D., Spiers, C. J., & Niemeijer, A. R. (2016). Understanding induced seismicity. *Science*, *354*(6318), 1380–1381. https://doi.org/10.1126/science.aal2584

Eyre, T. S., Eaton, D. W., Garagash, D. I., Zecevic, M., Venieri, M., Weir, R., & Lawton, D. C. (2019). The role of aseismic slip in hydraulic fracturing–induced seismicity. *Science Advances*, *5*(8), eaav7172. https://doi.org/10.1126/sciadv.aav7172

Fang, Y., Elsworth, D., Wang, C., Ishibashi, T., & Fitts, J. P. (2017). Frictional stability-permeability relationships for fractures in shales. *Journal of Geophysical Research: Solid Earth*, *122*, 1760–1776. https://doi.org/10.1002/2016JB013435

Fang, Y., Elsworth, D., Wang, C., & Jia, Y. (2018). Mineralogical controls on frictional strength, stability, and shear permeability evolution of fractures. *Journal of Geophysical Research: Solid Earth*, *123*, 3549–3563. https://doi.org/10.1029/2017JB015338

French, M. E., Zhu, W., & Banker, J. (2016). Fault slip controlled by stress path and fluid pressurization rate. *Geophysical Research Letters*, *43*, 4330–4339. https://doi.org/10.1002/2016GL068893

Guglielmi, Y., Cappa, F., Avouac, J. P., Henry, P., & Elsworth, D. (2015). Seismicity triggered by fluid injection-induced aseismic slip. *Science*, *348*(6240), 1224–1226. https://doi.org/10.1126/science.aab0476

Guo, T. (2013). Evaluation of highly thermally mature shale-gas reservoirs in complex structural parts of the Sichuan Basin. *Journal of Earth Science*, *24*(6), 863–873. https://doi.org/10.1007/s12583-013-0384-4

He, C., Tan, W., & Zhang, L. (2016). Comparing dry and wet friction of plagioclase: Implication to the mechanism of frictional evolution effect at hydrothermal conditions. *Journal of Geophysical Research: Solid Earth*, *121*, 6365–6383. https://doi.org/10.1002/2016JB012834

He, C., Yao, W., Wang, Z., & Zhou, Y. (2006). Strength and stability of frictional sliding of gabbro gouge at elevated temperatures. *Tectonophysics*, *427*(1–4), 217–229. https://doi.org/10.1016/j.tecto.2006.05.023

Hincks, T., Aspinall, W., Cooke, R., & Gernon, T. (2018). Oklahoma's induced seismicity strongly linked to wastewater injection depth. *Science*, *359*(6381), 1251–1255. https://doi.org/10.1126/science.aap7911

Hunfeld, L. B., Niemeijer, A. R., & Spiers, C. J. (2017). Frictional properties of simulated fault gouges from the seismogenic Groningen Gas Field under in situ P–T-chemical conditions. *Journal of Geophysical Research: Solid Earth*, *122*, 8969–8989. https://doi.org/10.1002/2017JB014876

Jiang, S., Xu, Z., Feng, Y., Zhang, J., Cai, D., Chen, L., et al. (2016). Geologic characteristics of hydrocarbon-bearing marine, transitional and lacustrine shales in China. *Journal of Asian Earth Sciences*, *115*, 404–418. https://doi.org/10.1016/j.jseaes.2015.10.016

King, D. S. H., & Marone, C. (2012). Frictional properties of olivine at high temperature with applications to the strength and dynamics of the oceanic lithosphere. *Journal of Geophysical Research*, *117*, B12203. https://doi.org/10.1029/2012JB009511

Kohli, A. H., & Zoback, M. D. (2013). Frictional properties of shale reservoir rocks. *Journal of Geophysical Research: Solid Earth*, *118*, 5109–5125. https://doi.org/10.1002/jgrb.50346

Lei, X., Huang, D., Su, J., Jiang, G., Wang, X., Wang, H., et al. (2017). Fault reactivation and earthquakes with magnitudes of up to M_w 4.7 induced by shale-gas hydraulic fracturing in Sichuan Basin, China. *Scientific Reports*, *7*(1), 1–12. https://doi.org/10.1038/s41598-017-08557-y

Lei, X., Wang, Z., & Su, J. (2019). The December 2018 M_L 5.7 and January 2019 M_L 5.3 earthquakes in south Sichuan Basin induced by shale gas hydraulic fracturing. *Seismological Research Letters*, *90*(3), 1099–1110. https://doi.org/10.1785/0220190029

Linker, M. F., & Dieterich, J. H. (1992). Effects of variable normal stress on rock friction: Observations and constitutive equations. *Journal of Geophysical Research*, *97*(B4), 4923. https://doi.org/10.1029/92JB00017

Logan, J. M., Dengo, C. A., Higgs, N. G., & Wang, Z. Z. (1992). Fabrics of experimental fault zones: Their development and relationship to mechanical behavior. In B. Evans, & T.-F. Wong (Eds.), *Fault mechanics and transport properties of rocks* (pp. 33–67). New York: Academic Press.

Lu, Z., & He, C. (2018). Friction of foliated fault gouge with a biotite interlayer at hydrothermal conditions. *Tectonophysics*, *740*, 72–92. https://doi.org/10.1016/j.tecto.2018.05.003

Marone, C. (1998). Laboratory-derived friction laws and their application to seismic faulting. *Annual Review of Earth and Planetary Sciences*, *26*(1), 643–696. https://doi.org/10.1146/annurev.earth.26.1.643

Marone, C., Raleigh, C. B., & Scholz, C. H. (1990). Frictional behavior and constitutive modeling of simulated fault gouge. *Journal of Geophysical Research*, *95*(B5), 7007–7025.

Martínez-Garzón, P., Kwiatek, G., Sone, H., Bohnhoff, M., Dresen, G., & Hartline, C. (2014). Spatiotemporal changes, faulting regimes, and source parameters of induced seismicity: A case study from the Geysers geothermal field. *Journal of Geophysical Research: Solid Earth*, *119*, 8378–8396. https://doi.org/10.1002/2014JB011385

Meng, L., McGarr, A., Zhou, L., & Zang, Y. (2019). An investigation of seismicity induced by hydraulic fracturing in the Sichuan Basin of China based on data from a temporary seismic network. *Bulletin of the Seismological Society of America*, *109*(1), 348–357. https://doi.org/10.1785/0120180310

Niemeijer, A. R., & Spiers, C. J. (2007). A microphysical model for strong velocity weakening in phyllosilicate-bearing fault gouges. *Journal of Geophysical Research*, *112*, B10405. https://doi.org/10.1029/2007JB005008

Paterson, M. S. (1995). A theory for granular flow accommodated by material transfer via an intergranular fluid. *Tectonophysics*, *245*(3–4), 135–151. https://doi.org/10.1016/0040-1951(94)00231-W

Pluymakers, A. M., & Niemeijer, A. R. (2015). Healing and sliding stability of simulated anhydrite fault gouge: Effects of water, temperature and CO_2. *Tectonophysics*, *656*, 111–130. https://doi.org/10.1016/j.tecto.2015.06.012

Rice, J. R., & Ruina, A. L. (1983). Stability of steady frictional slipping. *Journal of Applied Mechanics*, *50*(2), 343. https://doi.org/10.1115/1.3167042

Rubinstein, J. L., & Mahani, A. B. (2015). Myths and facts on wastewater injection, hydraulic fracturing, enhanced oil recovery, and induced seismicity. *Seismological Research Letters*, *86*(4), 1060–1067. https://doi.org/10.1785/0220150067

Ruina, A. (1983). Slip instability and state variable friction laws. *Journal of Geophysical Research*, *88*(B12), 10,359–10,370. https://doi.org/10.1029/JB088iB12p10359

Samuelson, J., Elsworth, D., & Marone, C. (2009). Shear-induced dilatancy of fluid-saturated faults: Experiment and theory. *Journal of Geophysical Research*, *114*, B12404. https://doi.org/10.1029/2008JB006273

Sawai, M., Niemeijer, A. R., Plümper, O., Hirose, T., & Spiers, C. J. (2016). Nucleation of frictional instability caused by fluid pressurization in subducted blueschist. *Geophysical Research Letters*, *43*, 2543–2551. https://doi.org/10.1002/2015GL067569

Scuderi, M. M., & Collettini, C. (2018). Fluid injection and the mechanics of frictional stability of shale-bearing faults. *Journal of Geophysical Research: Solid Earth*, *123*, 8364–8384. https://doi.org/10.1029/2018JB016084

Scuderi, M. M., Collettini, C., & Marone, C. (2017). Frictional stability and earthquake triggering during fluid pressure stimulation of an experimental fault. *Earth and Planetary Science Letters*, *477*, 84–96. https://doi.org/10.1016/j.epsl.2017.08.009

Tan, J., Weniger, P., Krooss, B., Merkel, A., Horsfield, B., Zhang, J., et al. (2014). Shale gas potential of the major marine shale formations in the Upper Yangtze Platform, South China, Part II: Methane sorption capacity. *Fuel*, *129*, 204–218. https://doi.org/10.1016/j.fuel.2014.03.064

van der Elst, N. J., Savage, H. M., Keranen, K. M., & Abers, G. A. (2013). Enhanced remote earthquake triggering at fluid-injection sites in the midwestern United States. *Science*, *341*(6142), 164–167. https://doi.org/10.1126/science.1238948

Westaway, R., & Burnside, N. M. (2019). Fault "corrosion" by fluid Injection: A potential cause of the November 2017 5.5 Korean Earthquake. *Geofluids*, *2019*, 1–23. https://doi.org/10.1155/2019/1280721

Xi, Y., Li, J., Liu, G., Cha, C., & Fu, Y. (2018). Numerical investigation for different casing deformation reasons in Weiyuan-Changning shale gas field during multistage hydraulic fracturing. *Journal of Petroleum Science and Engineering*, *163*, 691–702. https://doi.org/10.1016/j.petrol.2017.11.020

Xu, Z., Jiang, S., Yao, G., Liang, X., & Xiong, S. (2019). Tectonic and depositional setting of the lower Cambrian and lower Silurian marine shales in the Yangtze Platform, South China: Implications for shale gas exploration and production. *Journal of Asian Earth Sciences*, *170*, 1–19. https://doi.org/10.1016/j.jseaes.2018.10.023

Yeck, W. L., Hayes, G. P., McNamara, D. E., Rubinstein, J. L., Barnhart, W. D., Earle, P. S., & Benz, H. M. (2017). Oklahoma experiences largest earthquake during ongoing regional wastewater injection hazard mitigation efforts. *Geophysical Research Letters*, *44*, 711–717. https://doi.org/10.1002/2016GL071685

Zhang, F., An, M., Zhang, L., Fang, Y., & Elsworth, D. (2019). The role of mineral composition on the frictional and stability properties of powdered reservoir rocks. *Journal of Geophysical Research: Solid Earth*, *124*, 1480–1497. https://doi.org/10.1029/2018JB016174

Zhang, F., Fang, Y., Elsworth, D., Wang, C., & Yang, X. (2017). Evolution of friction and permeability in a propped fracture under shear. *Geofluids*, *2017*, 1–13. https://doi.org/10.1155/2017/2063747

Zhang, F., Yin, Z., Chen, Z., Maxwell, S., Zhang, L., & Wu, Y. (2019). Fault reactivation and induced seismicity during multi-stage hydraulic fracturing: Field microseismic analysis and geomechanical modeling. *SPE Journal*, *25*(02), 692–711. https://doi.org/10.2118/199883-PA

Zhang, L., He, C., Liu, Y., & Lin, J. (2017). Frictional properties of the South China Sea oceanic basalt and implications for strength of the Manila subduction seismogenic zone. *Marine Geology*, *394*, 16–29. https://doi.org/10.1016/j.margeo.2017.05.006

Zhao, L., Qin, X., Zhang, J., Liu, X., Han, D., Han, J. G., & Xiong, Y. (2017). An effective reservoir parameter for seismic characterization of organic shale reservoir. *Surveys in Geophysics*, *39*(3), 509–541. https://doi.org/10.1007/s10712-017-9456-9

Zou, C., Dong, D., Wang, Y., Li, X., Huang, J., Wang, S., et al. (2016). Shale gas in China: Characteristics, challenges and prospects (II). *Petroleum Exploration and Development*, *43*(2), 182–196. https://doi.org/10.1016/S1876-3804(16)30022-2